actuators

MDPI

Article

Research on Spatial Developable Mechanism Considering Revolute Clearance Joints with Irregular Rough Surfaces

Junyu Wang [1], Huibo Zhang [1,*], Wenyu Wang [1], Chaoqun Qi [2], Jianan Xu [1], Yang Zhao [3], Chao Ma [4] and Jian Tian [4]

[1] College of Mechanical and Electrical Engineering, Harbin Engineering University, Harbin 150001, China; wjy6255533@hrbeu.edu.cn (J.W.) ; wwy_42@hrbeu.edu.cn (W.W.); xujianan@hrbeu.edu.cn (J.X.)
[2] School of Mechanical Engineering, Hebei University of Technology, Tianjin 300130, China; 201911201014@stu.hebut.edu.cn
[3] Harbin Institute of Technology, Harbin 150001, China; yangzhao@hit.edu.cn
[4] Beijing Institute of Spacecraft System Engineering, Beijing 100094, China; machaodn@163.com (C.M.); tj15704618301@163.com (J.T.)
* Correspondence: zhanghuibo@hrbeu.edu.cn

Abstract: Due to assembling, manufacturing errors, and wear, irregular rough surfaces inevitably exist in joints, which will increase the contact stiffness nonlinearity at the joint of the spatial developable mechanism, and the traditional contact force model is difficult to accurately predict the contact force change of irregular rough surface clearance. Aiming at the difficulty of accurately predicting the dynamic behavior of the spatial developable mechanism caused by rough joint clearance, an improved clearance contact force modeling method based on an uncoordinated contact model is proposed in this paper. The influence of rough peak distribution on the contact area is analyzed. The stiffness of the traditional Hertz model is modified based on the probability distribution density function of the rough peak, and an improved contact force model based on dynamic contact stiffness is established. Based on the Lagrange multiplier method, the dynamics model of spatial developable mechanism is constructed. Based on the model, the dynamic analysis of the spatial expansion mechanism is carried out, and the influence of the roughness of the contact surface and the size of the clearance on the dynamic characteristics of the system are explored; as well, the influence of different clearance parameters on the dynamic characteristics of the development mechanism is revealed. Through the analysis, this paper provides a theoretical basis for predicting the effect of a spatial revolute clearance joint on the dynamic characteristics of the mechanism and lays a good foundation for the manufacture and application of the mechanism.

Keywords: spatial developable mechanism; irregular surfaces clearance; dynamic contact stiffness; mechanical system; dynamic characteristics

check for updates

Citation: Wang, J.; Zhang, H.; Wang, W.; Qi, C.; Xu, J.; Zhao, Y.; Ma, C.; Tian, J. Research on Spatial Developable Mechanism Considering Revolute Clearance Joints with Irregular Rough Surfaces. *Actuators* **2023**, *13*, 274. https://doi.org/10.3390/act13070274

Academic Editor: Ignazio Dimino

Received: 20 June 2024
Revised: 17 July 2024
Accepted: 19 July 2024
Published: 21 July 2024

Copyright: © 2023 by the authors. Licensee MDPI, Basel, Switzerland. This article is an open access article distributed under the terms and conditions of the Creative Commons Attribution (CC BY) license (https://creativecommons.org/licenses/by/4.0/).

1. Introduction

With the increasing demand for large-scale space deployable mechanisms such as large-scale antennas and solar panels, the requirement for the accuracy of the shape maintenance of their in-orbit services is constantly increasing. However, due to machining technology, assembly errors, and other reasons, the joint of the developing mechanism inevitably has a clearance of moving pairs, thus resulting in the flutter phenomenon, which then affects the shape accuracy of the developing mechanism. Therefore, in order to achieve high precision prediction and control of flutter, it is urgent to carry out refined dynamic modeling research of the spatial development mechanism with a clearance joint.

Aiming at the problem of modeling the contact force of the ideal smooth joint clearance, the contact can be divided into uncoordinated contact and conformal contact according to the contact state. Between them, the noncoordinated contact solves the modeling problem of joint contact force with large clearance. Among them, the continuous contact force model of the interstitial moving pair is widely used [1–4]. This model was first proposed by the

researcher Earles in the early 1970s [5]. The Hertz contact force model [6], L-N contact force model [7], and Flores contact force model [8] are the most authoritative continuous contact force models at present. Hertz et al. [9] put forward a normal contact force model that can accurately calculate the nonlinear contact force at the clearance between two contacts. In order to make up for the lack of energy loss in the Hertz contact model, Lankanani [10] proposed the L-N continuous contact force model, which introduced the viscous damping coefficient to describe the energy dissipation of the contact body during the contact process. This model provides a more accurate description of the motion of the contact. Based on the L-N continuous contact model, Flores [11] proposed a general modeling method for rotating joints with clearance in multibody systems. This method provides a new way to solve complex motion problems in multibody systems theoretically. With the continuous improvement of machining accuracy, the joint clearance of the mechanism gradually becomes smaller, and the joint contact state changes from noncoordinated contact to conformal contact. In this case, the traditional hypothesis of the noncoordinated contact theory is no longer applicable [12–16]. Therefore, researchers at home and abroad have carried out different research projects on the conformal contact of a joint space. Yan et al. [16,17] considered influence factors such as surface quality, axial bending deformation, and the viscous effect of moving pairs, which they combined with the Winkler elastic contact hypothesis and the traditional Hertz contact hypothesis; this model regarded the contact behavior under the condition of small clearance as a near-coordinated state, that is, there is a small clearance between contact surfaces. A near-coordinated contact force model for small clearances has been proposed. Based on the assumptions of the Winkler and Hertz contact models, Liu et al. [10,18,19] used geometric methods to deduce the contact boundary of spherical joints with clearances, and they established a conformal contact model that accurately described the contact state of spherical joints in the process of motion. The proposed model provides a new theoretical framework for solving the spherical joint contact problem with clearances.

However, all the contact force models listed above focus on the case of smooth surfaces; however, in the actual contact process, the contact surface is often not completely smooth, and the joints cannot be fully fitted, thus resulting in discontinuity of the contact surface. The contact state may change due to the slightly convex surface or irregular shape. This will cause local load concentration or uneven distribution of the contact surface and then affect the dynamic characteristics of the mechanism.

In terms of the contact characteristics of irregular surface joints, scholars have divided them into two types of description methods, named statistical description and classification description. Based on the statistical description, the scholars did the following research. Greenwood et al. [17,20] first studied rough contact surfaces and proposed the G-W model. Han et al. [21,22] proposed a multibody dynamic modeling method for joints with irregular rough clearance surfaces considering the elastic deformation of microconvex contact surfaces, and they proposed wear prediction and dynamic error analysis methods for joint contact surfaces. In order to make up for the defect of a single radius of curvature in the hemispherical model, Shang et al. [23,24] proposed the method of an equivalent microconvex of a parabolic rotary body to correct the deficiency of the traditional hypothesis of a hemispherical microconvex, and they deduced the relationship between the normal stiffness of rough surfaces and elastic contact. Li Ling et al. [25] further used the hypothesis that the rotating body of the quadratic function is equivalent to the traditional hemispherical microconvex body, and based on a rough surface topography measurement test, they established the analytical relationship between the contact radius and the contact deformation of a microconvex body. Wei Long et al. [26] introduced the advantages and disadvantages of the Hertz contact model, statistical contact model, and fractal contact model, respectively. Based on the classification description method, domestic and foreign scholars have conducted the following research. In 1990, Majumdar and Bhushan [27,28] jointly proposed a rough surface contact model based on fractal geometry theory, and they obtained a more realistic relationship between the contact area of microconvex bodies and

the contact load. In 2009, based on the fractal theory, Wen Shuhua et al. [29] introduced a contact area distribution function with the cross-sectional area of the deformation position of a microconvex body as a variable, and they established a fractal model of contact stiffness of the joint surface considering the region expansion factor.

According to the different precision requirements of the research objects, the main research methods adopted at this stage are different. For large developable mechanisms, such as solar panels, cranes, and space antennas, due to the large number of joints and large scale, the computational efficiency is required to be higher. At this stage, most of the statistical joint contact modeling is adopted, such as using the G-W model [30]. For high-precision transmission mechanisms with smaller scales and higher precision requirements, topography modeling such as the M-B modeling method [31] is generally adopted at this stage.

However, both the existing statistical contact force model and the fractal contact model have their limitations. The statistical contact force model does not study the mapping relationship between the overall embedding depth of the contact surface and the actual embedding depth, which makes it difficult to consider the energy loss caused by nonlinear damping and thus makes the error of the contact force model larger. The fractal contact model needs to first extract the real topography data of the rough surface of the object through the instrument and then calculate the rough surface of the object based on the fractal theory. Although the contact force of the rough surface can be accurately described, it is difficult to model the multijoint spatial expansion mechanism efficiently due to the large amount of calculation and the need to sample different contact surfaces.

Therefore, aiming at the problem that it is difficult for traditional contact models to accurately and efficiently describe the contact state of irregular rough clearance surfaces, an improved clearance contact force modeling method based on an uncoordinated contact model [1–4] is proposed in this paper. Firstly, the contact state is simplified by referring to the G-W model [17,20] hypothesis, and the contact force modeling is simplified into modeling the contact force of a single microconvex body, which is followed by statistical modeling. Then, the contact force of a single microconvex body is modeled based on the traditional Hertz model [6], and the stiffness of the traditional Hertzian model is modified based on the probability distribution density function of the rough peak. Based on the L-N model [7], the nonlinear damping term is introduced into the contact force calculation model, and an improved contact model based on dynamic contact stiffness is established. A multibody dynamics model based on the improved contact model is established for the space development mechanism. The improved contact model is explored and verified using dynamic simulation. The accuracy and superiority of the improved contact model are verified by comparing the simulation results.

The remaining work is organized as follows. Section 2 introduces the contact modeling, including the normal contact force model and the tangential friction force model . Section 3 proposes a method for estimating the dynamic modeling of the space expansion mechanism of irregular rough surface joints. In Section 4, the dynamic simulation analysis of the mechanism is carried out, and the dynamic response of different spacecraft components under different contact parameters is compared and analyzed. Furthermore, the optimal processing parameters of components with different requirements of the spatial developable mechanism are obtained. Finally, conclusions are drawn in the last section.

2. Consider Joint Contact Modeling for Irregular Rough Surfaces

In this section, the normal contact stiffness of joints with irregular rough surfaces is first modified based on the rough surface hypothesis; then, the hysteresis damping factor is introduced to consider the energy dissipation, and an improved normal contact force model based on dynamic contact stiffness is established. It solves the problem that the traditional contact model is difficult to accurately and efficiently describe the contact state of the irregular rough clearance surface, and it realizes the nonlinear fine description of the joint contact stiffness under the typical embedding depth.

The derivation roadmap is shown in Figure 1.

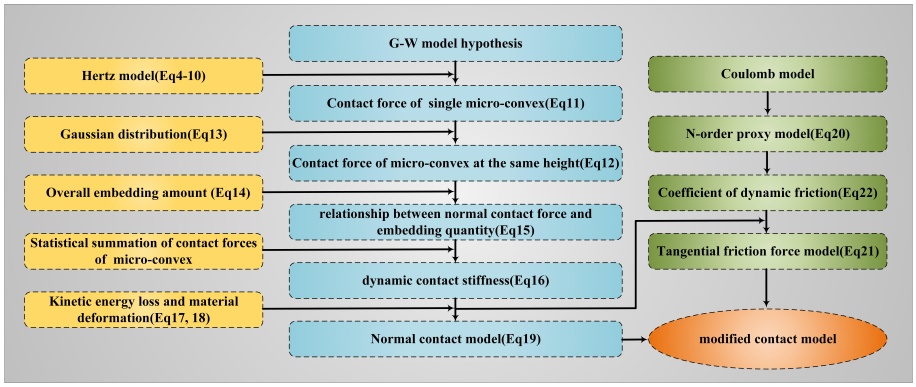


Figure 1. Flow chart of contact force.

The specific derivation process is as follows:

2.1. Contact State Determination

The schematic diagram of a rotating hinge on a rough surface is shown in Figure 2. Here, O_1 and O_2 are the center positions of the journals and bearings, respectively, R_1 and R_2 are the radius sizes of the journals and bearings, respectively, h is the height of the microconvex bodies, c is the clearance size, and $c = R_2 - R_1$ and e define the eccentricity distance of the journals relative to the bearings and $e = |O_1O_2|$.

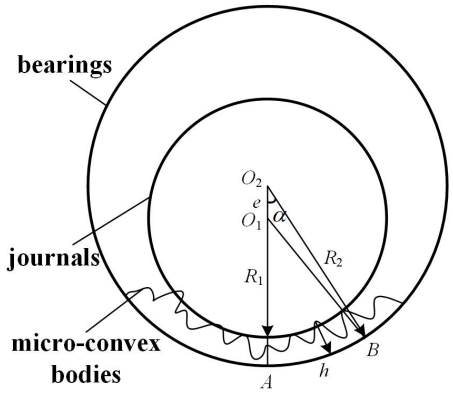


Figure 2. Schematic diagram of a rough rotating hinge with clearance.

Therefore, the amount of embedding produced by the collision is

$$\delta = e - (c - h) \tag{1}$$

According to the amount of δ embedding to judge the contact state at the hinge, the deformation is greater than zero, and collision contact occurs; on the contrary, the pin and the bushing are in a separate state. In order to describe the contact state, the state function $S(\delta)$ is introduced:

$$S(\delta) = \begin{cases} 1 & \delta \geq 0 \\ 0 & \delta < 0 \end{cases} \tag{2}$$

2.2. Normal Contact Force Model

As is shown in Figure 3 , this paper establishes a model with reference to the G-W model hypothesis [30]. The two contact surfaces are equivalent to the contact between a smooth rigid plane and a rough surface, and they obey two assumptions:

(1) It is supposed that the height of the microconvex body h on the rough contact surface follows the mean h_0 Gaussian distribution of $\phi(h)$.
(2) It is assumed that the tips of each microconvex body are hemispheres with curvature radii and are evenly distributed on the entire joint surface, as shown in the figure below.

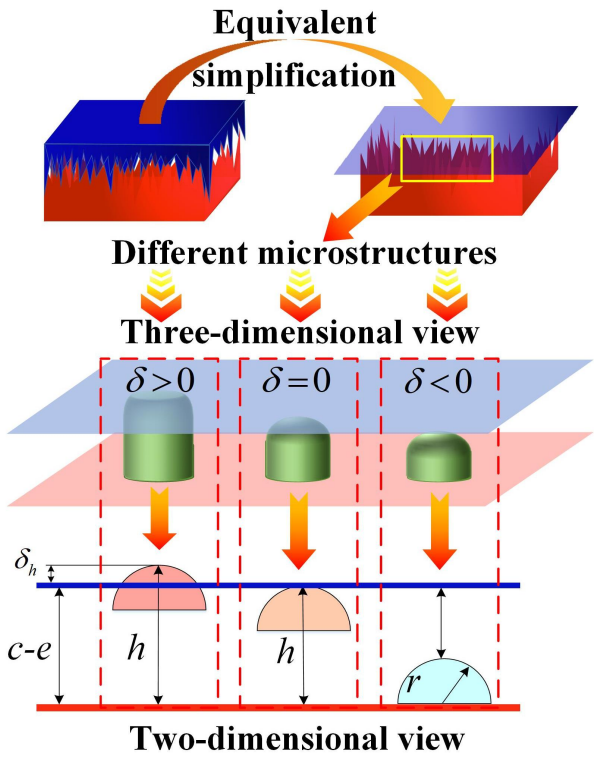


Figure 3. Microscopic diagram of rough contact surface.

Then, the contact force of a single microconvex body is modeled by simplifying the contact form of the contact surface into multiple microconvex bodies and the smooth plane. Finally, the contact stiffness of all microconvex bodies in contact is modeled statistically based on the probability density function to obtain the modified contact stiffness based on the overall embedding quantity. Since the height of the microconvex is not negative and follows the normal distribution whose mean value is h_0, the height range of the microconvex can be set as $[0, 2h_0]$, where the embedding quantity of a single microconvex is $\delta_h = e-(c-h)$, and the embedding amount of the first deformed microconvex body is set as the overall embedding amount, which is expressed as $\delta = e-(c-2h_0)$. The number density of the microconvex body in the contact area is

$$\eta = R\alpha/r \tag{3}$$

where r is the radius of the microconvex body, R is the contact radius, and α is the contact half angle.

Since the contact radius of the microconvex body is much smaller than that of the whole joint, the contact force of a single microconvex body can be calculated using the Hertz model. According to the Hertz theory [8], the expression of pressure distribution at any point in the contact area is as follows:

$$p(r_0) = p_0\left[1 - (r_0/a)^2\right]^{1/2} \tag{4}$$

where p_0 is the maximum stress value on the contact area; a is the width of the contact area; r_0 is the distance from the contact center; and $r_0 \leq a$. Since the surface or curve on

the contact interface is smooth and continuous on a macro level, the normal displacement boundary conditions in the contact region can be determined as

$$\bar{\boldsymbol{u}}_{z1} + \bar{\boldsymbol{u}}_{z2} = \delta - (1/2R_0){r_0}^2 \tag{5}$$

where $\bar{\boldsymbol{u}}_{\boldsymbol{zi}}$ is the normal displacement of the contact ball i (i = 1, 2) at the distance from the contact center caused by pressure; R_0 is the equivalent contact curvature; and $1/R_0 = 1/r \pm 1/R$. When the two balls are external contact, take the "+" sign; when the two balls are internal contact, take the "−" sign. Since r is much smaller than R, $R_0 \approx r$.

The normal displacement caused by pressure at point r, the distance from the contact center, can be calculated by the following formula:

$$\bar{\boldsymbol{u}}_{zr} = \frac{1-v^2}{E}\frac{\pi p_0}{4a}\left(2a^2 - r^2\right),\ r \le a \tag{6}$$

Combining the Equations (5) and (6), we can obtain the following:

$$\left(\frac{1-v_1^2}{E_1} + \frac{1-v_2^2}{E_2}\right)\frac{\pi p_0}{4a}\left(2a^2 - r^2\right) = \delta_h - (1/2R)r^2 \tag{7}$$

The composite elastic modulus is defined as E^*, and the contact circle radius can be obtained from Equation (7) as follows:

$$a = \frac{\pi p_0 R}{2E^*} \tag{8}$$

Based on the penetration hypothesis, the intrusion depth of the two contacts δ is

$$\delta_h = \frac{\pi a p_0}{2E^*} \tag{9}$$

The stress on the contact region is integrated in the contact region [0, a], and the relationship between the normal contact force and the embedding quantity is as follows:

$$F_N = \int_0^a p(r)2\pi r\mathrm{d}r = \frac{2}{3}\pi a^2 p_0 \tag{10}$$

Further integrating Equations (7)–(10) can obtain the relationship between the contact force and embedding quantity:

$$F_N = K{\delta_h}^n \tag{11}$$

where K is the stiffness coefficient of the collider, and $K = 4E^*R^{0.5}/3$; n is a power index related to the material properties of the contact, and the value of general metal materials is 1.5 [8].

After the contact force of a single microconvex body is obtained, the contact force generated by all the contact microconvex bodies each with a height of h is summed, and the relationship between the contact force and the height of h of the microconvex body is obtained as follows:

$$F_h = n_h F_N = \frac{4n_h E^* r^{0.5}{\delta_h}^{1.5}}{3} \tag{12}$$

$$n_h = \eta\varphi(h) \tag{13}$$

where n_h is the number of microconvex bodies with heights of h, δ_h is the embedding amount of microconvex bodies with heights of h, and the relationship between it and the overall embedding amount is as follows:

$$\delta_h = \delta - (2h_0 - h) \tag{14}$$

Finally, the normal contact of microconvex bodies with different heights resulting in deformation is sought, and the relationship between the normal contact force and the embedding quantity is obtained as follows:

$$F_N = \int_{2h_0-\delta}^{2h_0} F_n \mathrm{d}h = \eta^{0.5} \frac{\sqrt{\pi} 4R^{0.5} E^*}{3} \int_{2h_0-\delta}^{2h_0} \varphi(h)(\delta - 2h_0 + h)^{1.5} \mathrm{d}h = K_e \delta^{1.5} \tag{15}$$

where K_e is the dynamic contact stiffness, which is expressed as

$$K_e = \eta^{0.5} \frac{\sqrt{\pi} 4R^{0.5} E^*}{3\delta^{1.5}} \int_{2h_0-\delta}^{2h_0} \varphi(h)(\delta - 2h_0 + h)^{1.5} \mathrm{d}h \tag{16}$$

After correcting the dynamic contact stiffness and in order to accurately describe kinetic energy loss and material deformation based on the L-N model, this paper improved the dissipation term and introduced the nonlinear damping term into the contact force calculation model to reflect the change relationship between the contact force and the contact parameter. The expression is as follows: After correcting the dynamic contact stiffness, in order to accurately describe kinetic energy loss and material deformation based on the L-N model [7], this paper improved the dissipation term and introduced the nonlinear damping term into the contact force calculation model to reflect the change relationship between the contact force and the contact parameter. The expression is as follows:

$$F_N = K\delta^n + D_{L-N}\dot{\delta} \tag{17}$$

The damping coefficient expression is given as follows:

$$D_{L-N} = \frac{3K(1 - c_e^2)}{4\dot{\delta}^{(-)}} \delta^n \tag{18}$$

where K is the stiffness coefficient, $\dot{\delta}^{(-)}$ is the initial velocity, c_e is the recovery coefficient, and $c_e = v'/v_0$; v' is the postcollision velocity, and v_0 is the precollision velocity.

The dynamic contact stiffness replaces the contact stiffness of the traditional model, and a modified normal contact model is obtained.

$$F_N = K_e \delta^n (1 + \frac{3(1 - c_e^2)}{4\dot{\delta}^{(-)}} \dot{\delta}) \tag{19}$$

2.3. Tangential Friction Force Model

After the normal contact force modeling is completed, tangential friction modeling based on a modified Coulomb model is developed to solve the dry friction phenomenon between the space development mechanism in space environment. The friction model proposed by Coulomb is a classical model to describe the characteristics of dry friction, and the friction state is divided into static friction and dynamic friction, wherein the corresponding Coulomb friction model is established. However, the Coulomb model does not consider the effect of tangential velocity on tangential force, so it needs to be improved to adapt to the actual situation of mechanism motion in space environment. Dubowsky proposed a friction model considering normal contact, wherein the biggest limitation is that there is a jump phenomenon in the value of the friction. When the motion speed is zero, the solution of the friction will become very difficult. In this paper, the dynamic friction coefficient is further modified on the basis of the above friction model so that it can describe the friction behavior between rotating joints more accurately. Aiming at the step phenomenon of friction model, this paper establishes an n-order proxy model to correct the friction coefficient.

$$F(x) = y_2 - (y_2 - y_1)\left[\frac{(x - x_1)}{(x_2 - x_1)}\right]^{n-1}\left[n - (n-1)\frac{(x - x_1)}{(x_2 - x_1)}\right] \tag{20}$$

Equation (20) satisfies $F(x_1) = y_1$ and $F(x_2) = y_2$. (x_1, y_1) and (x_2, y_2) define the functional boundary condition, which in the friction model is (v_s, μ_s) and (v_d, μ_d). v_s is the static friction critical velocity, v_d is the maximum dynamic friction critical velocity, μ_d is the sliding friction coefficient, and μ_s is the static friction coefficient. Considering the model accuracy and calculation efficiency comprehensively, n was set to 3, so the modified tangential friction calculation formula is as follows:

$$F_t = -\mu(v_t)F_n\frac{v_t}{|v_t|} \tag{21}$$

where F_t is the tangential friction force; F_n is the normal positive pressure; $\mu(v_t)$ is the coefficient of dynamic friction; and v_t is the tangential velocity component. The calculation formula is the following:

$$\mu(v_t) = \begin{cases} -\mu_d sign(v_t) & |v_t| > v_d \\ -\left\{\mu_d + (\mu_s - \mu_d)\left(\frac{|v_t| - v_s}{v_d - v_s}\right)^2\left[3 - 2\left(\frac{|v_t| - v_s}{v_d - v_s}\right)\right]\right\} sign(v_t) & v_s \le |v_t| \le v_d \\ \mu_s - 2\mu_s\left(\frac{v_t + v_s}{2v_s}\right)^2\left(3 - \frac{v_t + v_s}{v_s}\right) & |v_t| < v_s \end{cases} \tag{22}$$

2.4. Model Verification

This section mainly verifies the accuracy of the above contact model. Since the finite element model can calculate single-joint contact force with high precision, the numerical simulation results of the single-joint modified model are compared with the finite element model and the traditional G-W model to verify the effectiveness of the model. Specific simulation parameters are shown in Table 1.

Table 1. Simulation numerical table of modified contact force model.

Parameter	Value
E	180 Gpa
C_e	0.85
v	0.35
R_a	3.2 μm
r	8.395 μm
R_1	4.9 μm
R_2	5 μm

Under a series of simulation parameters set in Table 1, dynamic simulation was performed by comparing the traditional G-W model, finite element model, and modified contact model, and simulation results of different contact models were obtained, as shown in Figure 4.

At present, there is no good direct measurement method for the joint contact force, so the finite element model with high accuracy was used to describe the joint contact force. Since the accuracy of the finite element model was the highest, we chose the finite element model as the basis, compared the traditional G-W model and the modified model proposed in this paper with the finite element model, respectively, and took the difference of the relative finite element model and the ratio of the finite element model as the model error for analysis and comparison [32–34]. As can be seen from Figures 4 and 5, compared to the G-W model, the error of the contact force change curve of the modified model and that of the finite element model increased with the increase in the embedding depth δ, but it was always smaller than that of the G-W model. Therefore, compared to the G-W model, the modified model proposed in this paper can describe the contact state of

irregular rough surfaces more accurately, and the smaller the embedding depth, the higher the prediction accuracy.

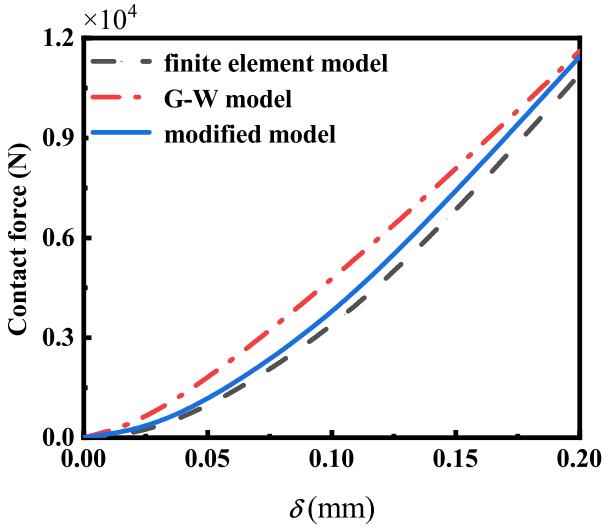


Figure 4. Comparison of contact models with different contact models.

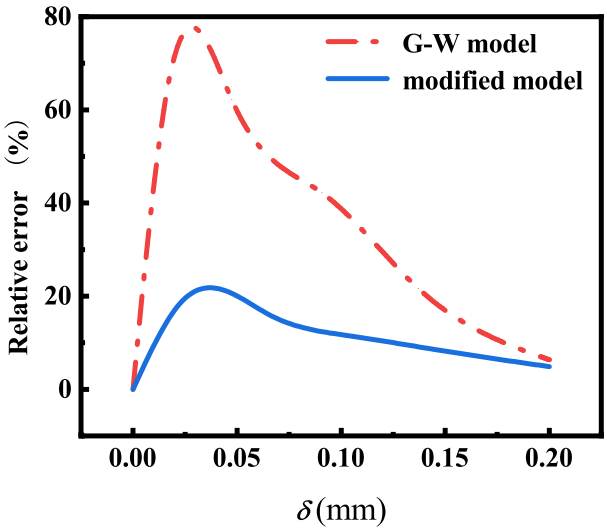


Figure 5. Error relative to the finite element model.

3. Considering the Dynamic Modeling of Space Expansion Mechanism of Irregular Rough Surface Joints

Since the space deployable mechanism has more demands on solar panels at this stage, the deployable mechanism model adopted in this chapter is shown in Figures 6 and 7, thus including the spacecraft body, two solar panels, and several connecting support rods. In the process of unfolding, although the mechanism is a three-dimensional space mechanism, there is no movement in the Z direction, because all points on the component move in the corresponding X–Y plane. Therefore, in this chapter, the deployable mechanism model was simplified to the X–Y plane projection of the mechanism to study the effect of joint clearance on the dynamic characteristics of the deployable mechanism.

In accordance with the behavior of the mechanism during unfolding, the mechanism was projected onto the X–Y plane, and the schematic diagram of the mechanism development process as shown in Figure 8 was obtained, thus indicating the motion process of the mechanism from the semiexpansion state to the expansion state, where l_9 is panel 1, l_9 is panel 2.

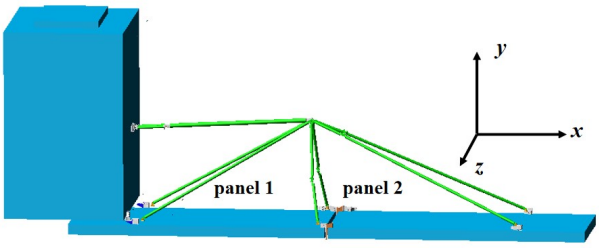


Figure 6. Schematic diagram of the structure of the spatial developable mechanism.

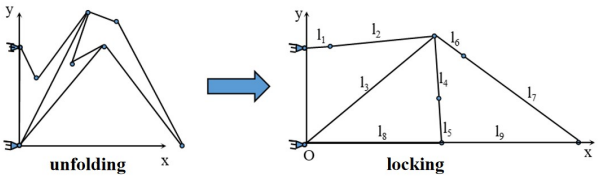


Figure 7. Schematic diagram of the spatial developable mechanism deployment process.

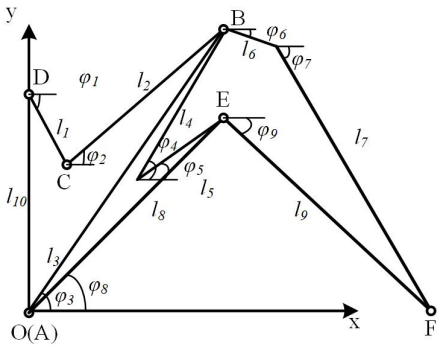


Figure 8. Schematic diagram of the spatial developable mechanism parameter diagram.

The mechanism is composed of three-ring mechanisms. According to the Lagrange multiplier modeling method, the closed-ring constraint equation of the mechanism is given as follows:

$$\begin{cases} l_1\cos\varphi_1 - l_2\cos\varphi_2 - l_3\cos\varphi_3 = 0 \\ l_1\sin\varphi_1 - l_2\sin\varphi_2 - l_3\sin\varphi_3 = -l_{10} \\ l_3\cos\varphi_3 - l_4\cos\varphi_4 - l_5\cos\varphi_5 = 0 \\ l_3\sin\varphi_3 - l_4\sin\varphi_4 - l_5\sin\varphi_5 = -l_8 \\ l_6\cos\varphi_6 + l_7\cos\varphi_7 - l_4\cos\varphi_4 - l_5\cos\varphi_5 - l_9\cos\varphi_9 = 0 \\ l_6\sin\varphi_6 + l_7\sin\varphi_7 - l_4\sin\varphi_4 - l_5\sin\varphi_5 - l_9\sin\varphi_9 = 0 \\ f_2(\phi) = f_1(\alpha) \\ f_8(\phi) = f_8(\alpha) \\ f_9(\phi) = f_9(\alpha) \end{cases} \tag{23}$$

where the kinetic energy of each connecting rod can be expressed as follows:

$$E_i = \frac{1}{2}m_i c_i^2 + \frac{1}{2}J_i\dot{\varphi}_i^2 = \frac{1}{2}\left[m_i\left(c_{ix}^2 + c_{iy}^2\right) + J_i\dot{\varphi}_i^2\right] \quad (i = [1, 2, \cdots, n]) \tag{24}$$

where c_{ix} and c_{iy} respectively represent the velocity of the center of mass of l_i in the direction of x and y, and m_i is the mass of l_i. The total kinetic energy of the developing mechanism composed of n poles is expressed as follows:

$$E_k = \sum_{i=1}^{n} E_i \tag{25}$$

The initial locking state of the spring of the space expansion mechanism is regarded as the initial state of energy storage. In the process of expansion, the spring will release the stored energy to drive the expansion of the space expansion unit. The nonlinear function of the coil spring development angle can be expressed as follows:

$$k_j = k_1\alpha + k_2\alpha^2 + k_3\alpha^3 \tag{26}$$

where k_j is the stiffness coefficient of the coil spring, and a is the angle of the coil spring development.

The spring elastic potential energy can be expressed as follows:

$$E_{pj} = E_p - k_j\alpha \tag{27}$$

The closed-loop constraint equation was used to solve the position of each azimuth angle of the expansion mechanism, and the Lagrange equation was used to model the dynamics of the space expansion mechanism. The dynamics equation of the expansion mechanism can be expressed as follows:

$$\frac{d}{dt}\left(\frac{\partial L}{\partial \dot{\varphi}_i}\right) - \frac{\partial L}{\partial \varphi_i} = F_i + [F_c] \quad (i = 1, 2, 3, \cdots, n) \tag{28}$$

where L is the Lagrange function—defined as the difference between the kinetic energy and potential energy of the space expansion element—ϕ_i is the generalized coordinate, F_i is the generalized force corresponding to the generalized coordinate, and $[F_c]$ is the resultant force of the normal contact force and tangential friction force. The Lagrange dynamics equation of the expansion element can be written in matrix form as follows:

$$\begin{cases} M\ddot{\varphi} + C\dot{\varphi} + K\varphi = F_i + [F_c] \\ \phi(\varphi, t) = 0 \end{cases} \tag{29}$$

where $\boldsymbol{K}$ is the generalized mass matrix, $\boldsymbol{C}$ is the generalized damping matrix, and $\boldsymbol{K}$ is the generalized stiffness matrix; m_{ij}, c_{ij}, k_{ij} represent the mass coefficient, damping coefficient, and stiffness coefficient of the superimposed expansion element, respectively.

In this paper, the generalized alpha method was used to solve the dynamic equation, and the specific simulation results are analyzed in the next section [35].

4. The Dynamic Characteristic Analysis of the Expansion Mechanism

In this section, the dynamic simulation analysis of the mechanism is carried out. The specific parameters of the expansion mechanism are shown in Table 2.

Table 2. The parameters of the developable mechanism.

	l_1	l_2	l_3	l_4	l_5
Length (mm)	450.32	2094.75	2805.04	841.54	636.0493
Quality (kg)	0.694	3.231	4.326	1.298	0.981
E (N/mm^2)			71,705		
	l_6	l_7	l_8	l_9	
Length (mm)	533.15	2844.25	2692.54	2692.54	
Quality (kg)	0.823	4.387	6.217	6.217	
E (N/mm^2)			71,705		

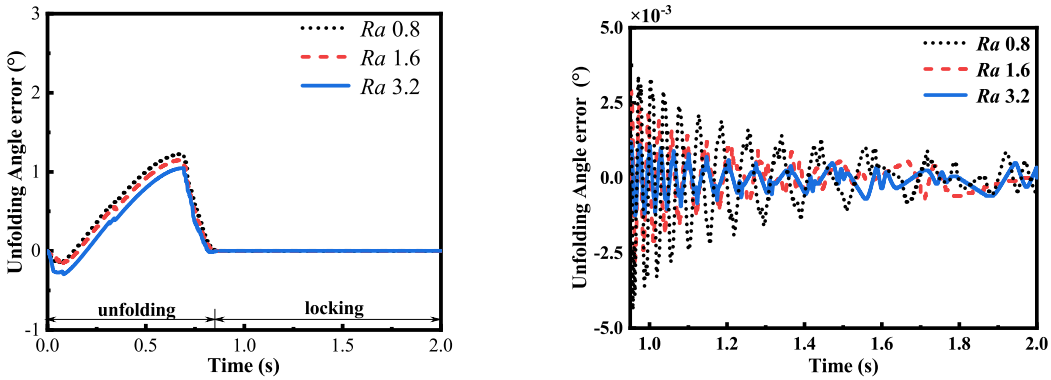
In the nonideal joint mechanism, the roughness of the clearance contact surface was set to an Ra of 0.8, an Ra of 1.6, and an Ra of 3.2 from fine to coarse. In addition, the clearance size from small to large was set to 0.01 mm, 0.05 mm, and 0.1 mm in turn. The simulation time was set to 2 s, the simulation step was set to 0.01 s, and the angle between panel 1 and y axis was set as the unfolding angle. When the mechanism unfolding angle reaches 90 deg, the mechanism locks. Then, the effects of different clearance parameters on the dynamics

of the deployable mechanism during the deployable and in-orbit phases can be analyzed in detail.

4.1. *Influence of Clearance Contact Surface Roughness on System Motion*

The spatial expansion mechanism starts to expand after it arrives at the working environment. The whole development stage is divided into a dynamic expansion process and a locking process after deployment. Therefore, for the nonideal joint mechanism, when the clearance size was 0.05 mm, the roughness of the clearance contact surface was set to an *Ra* of 0.8, an *Ra* of 1.6, and an *Ra* of 3.2 from fine to coarse to carry out simulation analysis.

Firstly, the deviation of the unfolding angle in the unfolding and locking processes under different roughness was compared. As can be seen in Figure 9, with the increase in the contact surface roughness, the angle deviation in the unfolding stage presented a trend of first increasing and then decreasing, while there was no significant difference between the upper and lower deviation ranges of the unfolding angle in the locking stage. The increase in the unfolding angle deviation in the initial development stage may be due to the increase in the initial friction force caused by the increase in roughness, which makes the mechanism need to overcome greater friction force to develop. With the development process, the reduction of contact force and the shortening of collision time caused by the increase of roughness effectively enhance the dynamic response speed of the system, thus making the deviation lower than that of the surface with low roughness.



(**a**) Unfolding angle error of mechanism in all stages

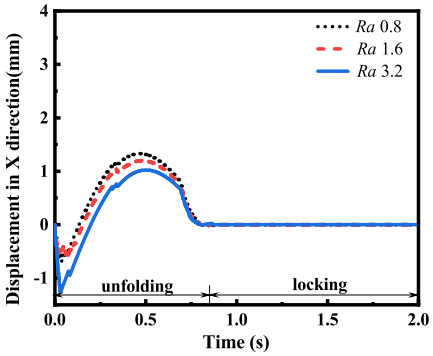
(**b**) Partial enlarged curve of mechanism locking phase

Figure 9. Unfolding angle error of mechanism in all stages.

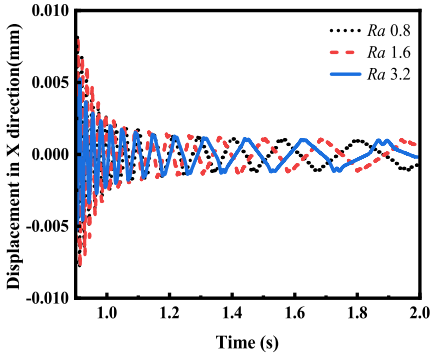
In addition, it can be seen from Figure 9b that, in the postlocking stage of the mechanism, the development angle deviation attenuated faster with the increase in roughness, which is because the increase in roughness is conducive to the surface microconvex body absorbing the collision energy between the elements of the motion amplitude so that the mechanism becomes stable faster.

Then, the displacement deviation of panel 1 and panel 2 under different roughness values was analyzed. Figures 10–13 show that in the development stage, the smaller the joint roughness, the greater the displacement deviation generated by the panel. In the locking stage, the smaller the roughness, the larger the flutter amplitude of the mechanism locking moment, but when the mechanism gradually became stable, the flutter amplitude of the different roughness values was basically similar. According to the analysis, this is because in the development stage of the developing mechanism, the force at the joint is larger, and the contact deformation generated by the collision is larger. Therefore, the contact force at the joint will have a greater impact on the structure, and the greater the roughness, the greater the contact force at the joint, and the more obvious the damping effect on the movement of the mechanism. In the locking stage, the impact force caused by the locking instantaneous impact still has a great influence. However, as the internal motion of the stable joint of the mechanism decreases, the force decreases. At this time, the

flutter effect of the solar panel is mainly affected by the overall flutter of the mechanism, and the impact of the contact force at the joint on the mechanism is basically ignored.

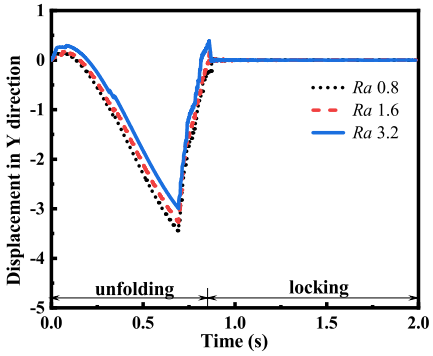


(**a**) Displacement deviation in the X direction at the end of panel 1

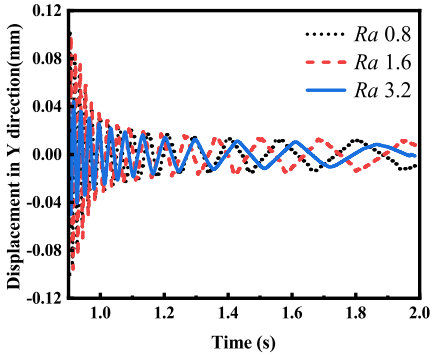


(**b**) Partial enlarged curve of mechanism locking phase

Figure 10. The fluctuation curve of displacement deviation in X direction of panel 1 under different roughness values.

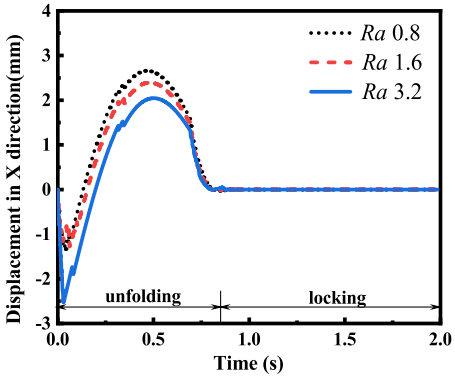


(**a**) Displacement deviation in the Y direction at the end of panel 1

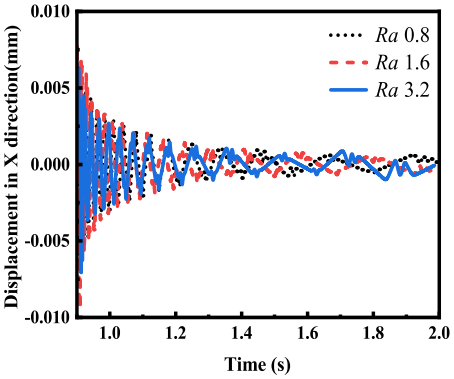


(**b**) Partial enlarged curve of mechanism locking phase

Figure 11. The fluctuation curve of displacement deviation in Y direction of panel 1 under different roughness values.

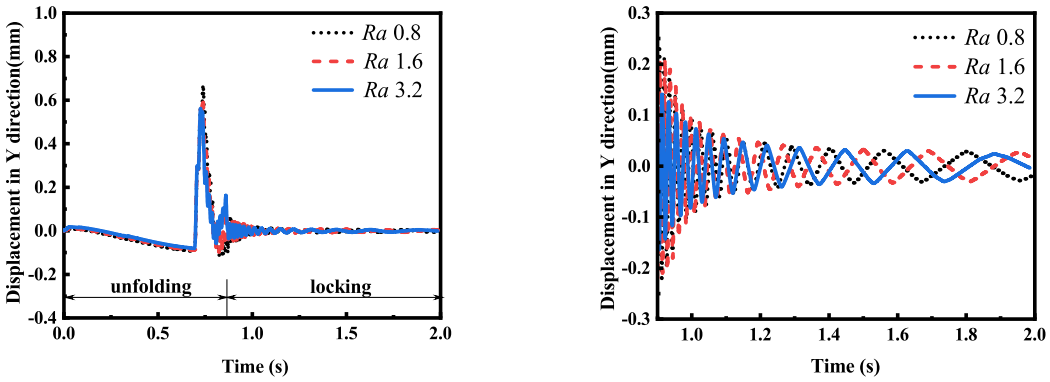


(**a**) Displacement deviation in the X direction at the end of panel 2



(**b**) Partial enlarged curve of mechanism locking phase

Figure 12. The fluctuation curve of displacement deviation in X direction of panel 2 under different roughness values.



(**a**) Displacement deviation in the Y direction at the end of panel 2

(**b**) Partial enlarged curve of mechanism locking phase

Figure 13. The fluctuation curve of displacement deviation in Y direction of panel 2 under different roughness values.

By comparing the simulation results in Figures 10a and 12a, it can be seen that the displacement deviations of panel 1 and panel 2 in the X direction were similar in the development stage, and the displacement deviation of panel 2X was about twice the deviation of panel 1. By comparing the simulation results in Figures 11a and 13a, it can be seen that the displacement deviations of panel 1 and panel 2 in the Y direction were not similar, and the deviation of the 2Y direction of the panel was smaller. The analysis suggests that this is because the panel has several support rods as constraints in the Y direction, and there is no additional support in the X direction, so the displacement deviation in the X direction will be superimposed with the superposition of the panel.

Compared to the simulation results in Figures 10b and 12b, it can be seen that the displacement deviation in the X direction of the end of panel 2 decayed faster after locking, and the displacement deviation in the X direction was lower than that in the 1X direction of the panel after relative stability. By comparing the simulation results in Figures 11b and 13b, it can be seen that the displacement deviation in the Y direction of panel 2 after stabilization was larger than that of panel 1. This is because there are relatively few support rods connected with panel 2, and they are subject to less locking torque after locking, so they can reach a stable state faster. However, due to the restriction, and panel 1 has a greater constraint in the Y direction than panel 2, panel 2 has worse stability in the Y direction than panel 1.

Transverse comparison of the joint spectrum under different roughness values shows the acceleration spectrum diagram of panel 1, as shown in Figure 14. It can be seen from the diagram that as the roughness of the contact surface continued to increase, the vibration amplitude of panel 1 first increased and then decreased, while the vibration amplitude frequency kept decreasing. When the roughness was an *Ra* of 0.8, the vibration peak was the lowest, and the vibration amplitude frequency was the lowest. At this time, the system was relatively stable, and the vibration was not obvious, but the vibration at low frequency can easily cause structural damage, and the energy transmission speed will be slower. When the roughness was an *Ra* of 1.6, the vibration crest was the largest, and the change of the peak and trough was the most obvious, thus indicating that the roughness of an *Ra* of 1.6 has obvious vibration phenomenon, which can effectively help to identify and evaluate the dynamic characteristics of the system. Furthermore, the vibration amplitude frequency was the highest, and the system response speed was faster. As a moving part directly connected to the spacecraft, panel 1 needs a faster system response speed to meet the needs of rapid response in the process of spacecraft movement, so in the design process, the roughness of panel 1 needs to be selected as an *Ra* of 1.6.

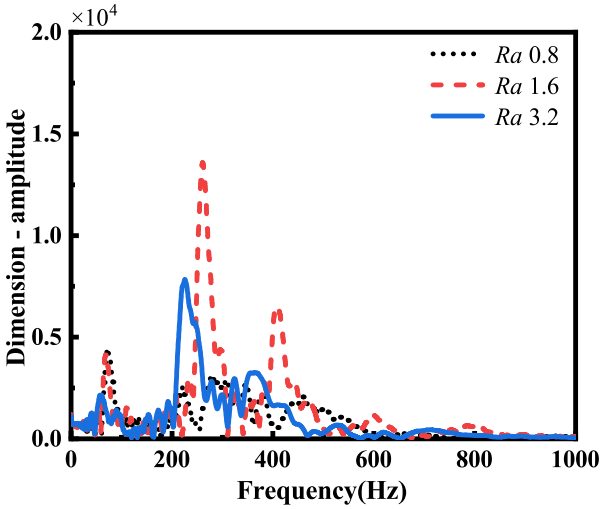


Figure 14. Acceleration spectrogram of panel 1 under different roughness values.

Figure 15 shows the acceleration spectrum of panel 2. It can be seen from the figure that the vibration amplitude of panel 2 varied similarly under different roughness conditions, and the vibration frequency was mainly between 90 Hz and 100 Hz. However, as the roughness increased, the vibration peak of panel 2 tended to increase first and then decrease; therefore, the larger the roughness is, the faster the attenuation speed will be. When the roughness was an *Ra* of 3.2, it had the fastest attenuation speed and lowest vibration peak. Therefore, the system has higher damping at this time, the vibration can dissipate faster, and the dynamic response of the system will be more stable. As the end transmission part of the expansion mechanism, panel 2 needs to reduce the vibration phenomenon of the system as much as possible to ensure the stability and reliability of the system operation. Therefore, in the design process, the roughness of panel 2 should be selected as an *Ra* of 3.2.

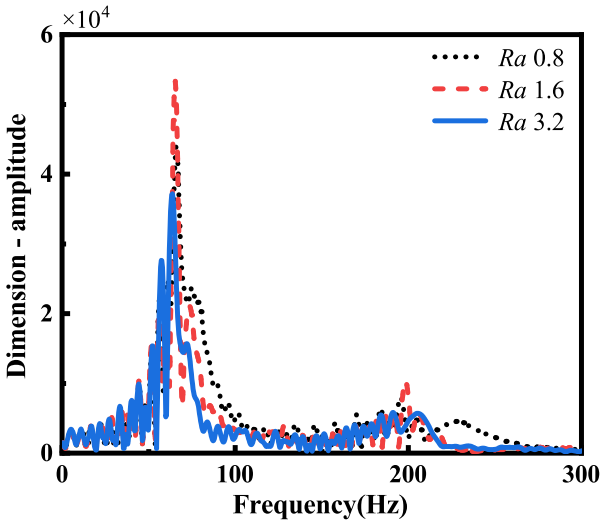
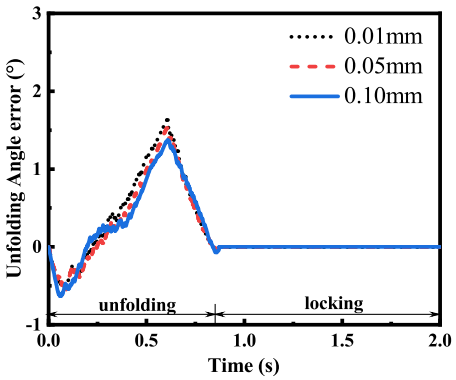


Figure 15. Acceleration spectrogram of panel 2 under different roughness conditions.

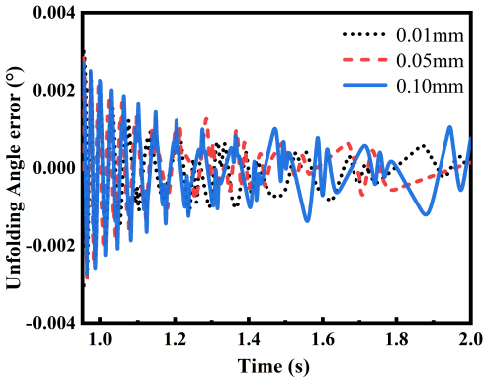
4.2. Analysis of the Influence of Rough Clearance Surface Clearance Size on System Motion Parameters

The spatial expansion mechanism starts to expand after it arrives at the working environment. The whole development stage is divided into a dynamic expansion process and a locking process after deployment. Since the typical roughness of the joint of the spatial expansion mechanism is an *Ra* of 1.6, we set the clearance size of the nonideal joint mechanism as 0.01 mm in turn when the roughness was at *Ra* values of 1.6 mm, 0.05 mm, and 0.1 mm. We then conducted simulation analysis.

Figure 16a shows that the range of the unfolding angle deviation decreases with the increase in the clearance size in the unfolding stage, and we found that the attenuation speed of the angular deviation increased with the increase in the clearance in the locking stage. This is because in the process of development, too small a joint clearance will enhance the collision phenomenon of the joint shaft pin, thus resulting in the mechanism being more prone to unstable motion in the development stage and increasing the deviation range of the development angle. After locking, as shown in Figure 16b, a large clearance reduced the damping effect of the mechanism, reduced the stability of the mechanism after locking, and increased the attenuation speed of the angle deviation.



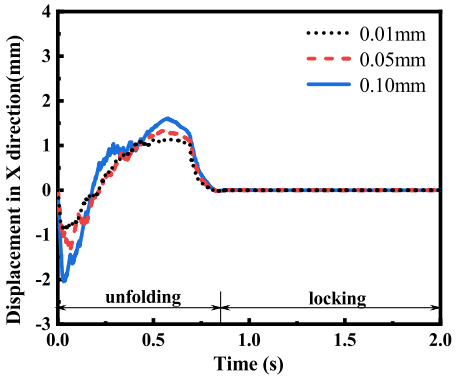
(**a**) Unfolding angle error of mechanism in all stages



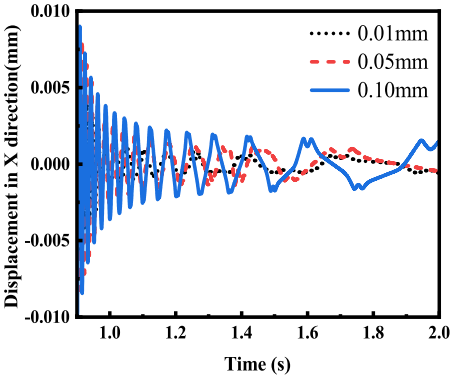
(**b**) Partial enlarged curve of mechanism locking phase

Figure 16. Unfolding angle error of mechanism in all stages.

Figures 17–20 show that in the expansion stage of the mechanism, as the clearance increased, the displacement deviation range of the X and Y directions between panel 1 and panel 2 increased. This is because a larger clearance will reduce the constraints of the panel in the development process, thus resulting in a larger shift of the panel. In the process of expansion, the clearance change has the least influence on the displacement deviation of the panel in the Y direction, so the panel has higher stability in the Y direction during the development process. In the locking stage of the mechanism, the stability of panel 2 becomes worse after the mechanism is stabilized due to the high tilt degree of its support rod 6 and support rod 7 after the mechanism is fully unlocked.

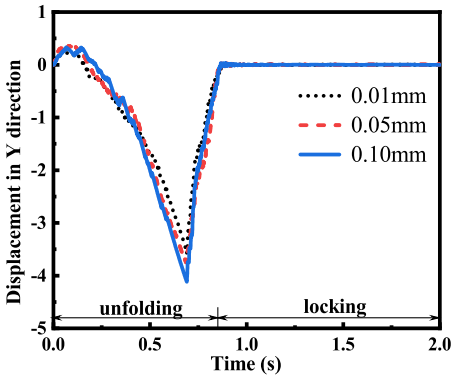


(**a**) Displacement deviation in the X direction at the end of panel 1

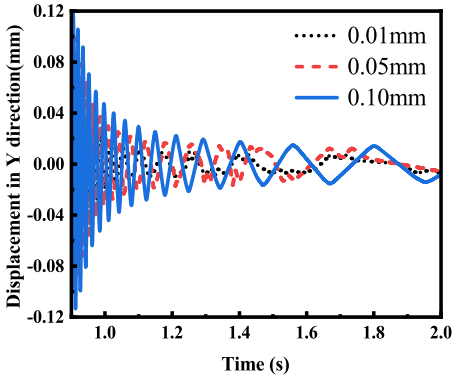


(**b**) Partial enlarged curve of mechanism locking phase

Figure 17. The fluctuation curve of displacement deviation in X direction of panel 1 under different clearance sizes.

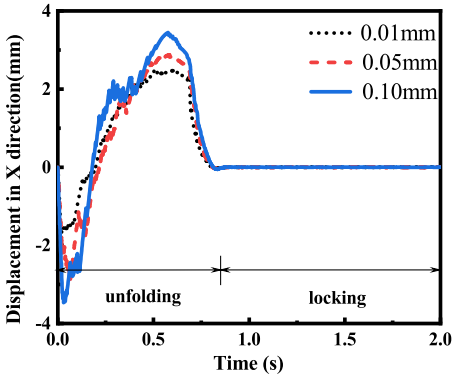


(**a**) Displacement deviation in the Y direction at the end of panel 1

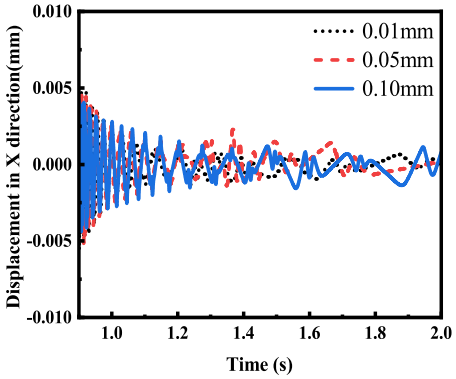


(**b**) Partial enlarged curve of mechanism locking phase

Figure 18. The fluctuation curve of displacement deviation in Y direction of panel 1 under different clearance sizes.

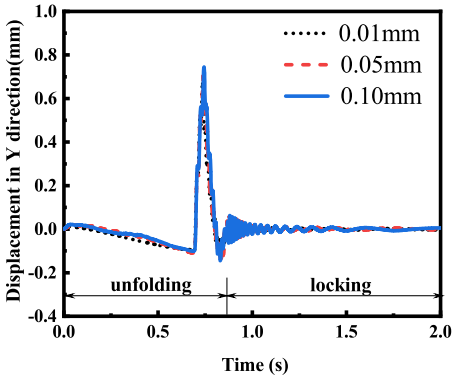


(**a**) Displacement deviation in the X direction at the end of panel 2

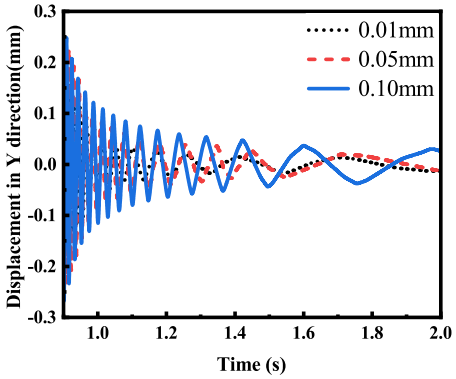


(**b**) Partial enlarged curve of mechanism locking phase

Figure 19. The fluctuation curve of displacement deviation in X direction of panel 2 under different clearance sizes.



(**a**) Displacement deviation in the Y direction at the end of panel 2



(**b**) Partial enlarged curve of mechanism locking phase

Figure 20. The fluctuation curve of displacement deviation in Y direction of panel 2 under different clearance sizes.

Figure 21 shows the acceleration spectrum diagram of panel 1 under different clearance sizes. With the increase in the clearance in the process of expansion, it can be observed that the peak height of the vibration spectrum diagram decreased, and the peak became more fuzzy, which means that with the increase in the clearance, the amplitude of the vibration

decreases, and the spectral resolution of the vibration signal decreases. At the same time, with the decrease in the clearance, the vibration amplitude peak lagged, thus indicating that the vibration response time of the system becomes longer. For smaller clearances, the vibration amplitude curve shows obvious fluctuation around 600 Hz, which indicates that the main vibration characteristics of the system were concentrated before 600 Hz, and the vibration mode of the system became more complex at higher frequencies.

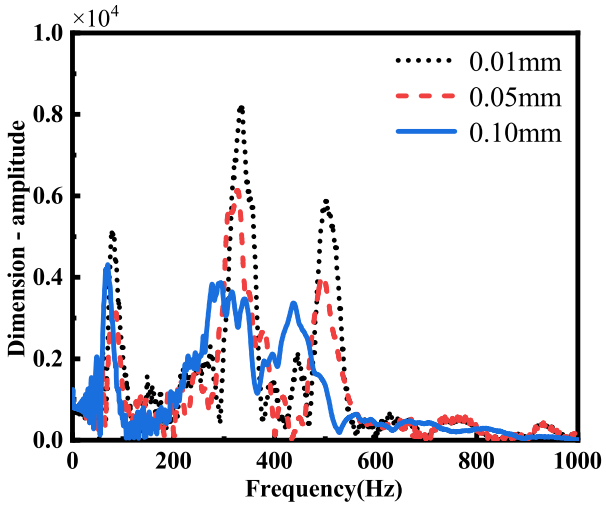


Figure 21. Acceleration spectrogram of panel 1 under different clearance sizes.

Figure 22 shows the acceleration spectrum diagram of panel 2 under different clearance sizes. With the increase in clearance, the peak of the vibration amplitude, frequency of vibration amplitude, and attenuation rate showed a trend of first increasing and then decreasing. This may be because the natural frequency of the system changes with the increase in the clearance, thus resulting in the increase in the vibration amplitude peak and vibration amplitude frequency. However, with the continuous increase in the clearance, different damping effects appeared, thus resulting in the decrease in the vibration amplitude peak, vibration amplitude frequency, and attenuation rate. By comparing Figures 21 and 22, the amplitude of the vibration is demonstrated to have increased with the increase in the series of panels, but the corresponding frequency of the vibration peaks decreased, and the number of wave peaks decreased significantly and became more concentrated.

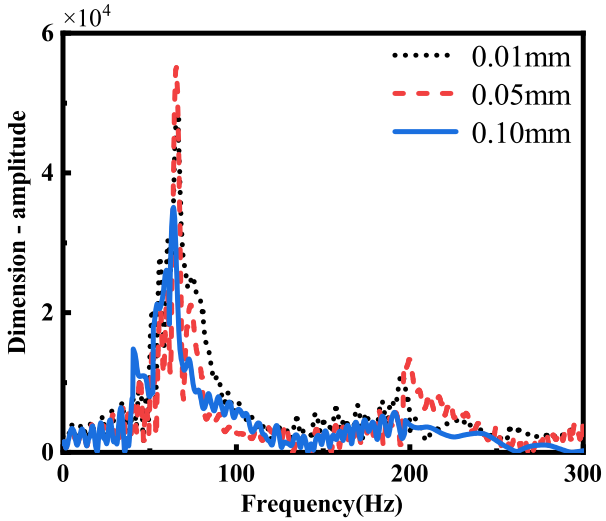


Figure 22. Acceleration spectrogram of panel 2 under different clearance sizes.

5. Conclusions

In this paper, an improved clearance contact force modeling method based on an uncoordinated contact model has been proposed, and based on the established dynamic model of the development mechanism, the dynamics analysis of the space development mechanism was carried out. The effects of contact surface roughness and clearance size on the system dynamics characteristics were investigated, and the influence of different clearance parameters on the dynamics characteristics of the development mechanism was revealed. The research results of this paper mainly include the following aspects:

1. To solve the problem that a single-contact model has difficulty describing the dynamic contact process, the contact stiffness was modified based on the rough surface hypothesis, and then the hystere-damping factor was introduced to consider the energy dissipation. An improved normal contact force model based on the dynamic contact stiffness was established, and a joint contact model considering irregular rough surfaces was constructed by combining the modified friction model. Compared to the G-W model and finite element model, it is concluded that the modified model is closer to the finite element model and has higher accuracy than the traditional G-W model.
2. Based on the established modified model, simulation research was conducted on the development mechanism, and the influence law of different contact surface roughness conditions and clearance sizes on the dynamics of the development mechanism was obtained. The dynamic response of different spacecraft components under different contact parameters was compared and analyzed, and the optimal processing parameters of components with different requirements of the space development mechanism were obtained. The optimal processing parameters can satisfiy the requirements of stability, response speed, and shape retention accuracy of the space development mechanism at the same time and provide a theoretical basis for the fine design of spacecraft.

In view of the existing methods and the unsolved problems in the analysis process, the future work of this topic can be selected from the following aspects:

1. In the actual work process, the linkage of the mechanism is not in a rigid body state for a long time, so the rigid–flexible coupling expansion mechanism model could be established considering the flexibility of the linkage so as to describe the behavior of the expansion mechanism in practical engineering applications more accurately.
2. This paper only focused on the dynamic modeling and dynamic response analysis of the two-stage deployable mechanism. With the continuous improvement of spacecraft functional requirements, the scale requirements of the space deployable mechanism will also increase, so it is urgent to carry out the dynamic modeling research of the multistage superimposed spatial developable mechanism. It provides a more perfect theoretical basis for the dynamic analysis and control of a large-scale multistage spatial expansion mechanism system.

Author Contributions: Methodology, H.Z.; formal analysis, W.W.; investigation and writing—original draft preparation, J.W.; writing—review and editing, J.W., H.Z. and C.Q.; supervision, J.X., Y.Z., C.M. and J.T. All authors have read and agreed to the published version of the manuscript.

Funding: This work was financially supported by the National Natural Science Foundation of China (Number U21B2075), the National Key R&D Program of China (Number 2023YFC2205900, 2023YFC2205903), the Reusable Space Debris Capture and Removal Project (Number KJSP2020010302), the Stable Supporting Fund of National Key Laboratory of Underwater Acoustic Technology (Number JCKYS2023604SSJS012), the Fundamental Research Funds for the Central Universities (Number 3072023WD070101), and the National Natural Science Foundation of China (Number 52375025).

Data Availability Statement: The original contributions presented in the study are included in the article material, further inquiries can be directed to the corresponding author.

Acknowledgments: We give thanks to the Harbin Engineering University and the Beijing Institute of Spacecraft System Engineering for their financial and equipment support for this project.

Conflicts of Interest: The authors declare no conflicts of interest.

References

1. Lai, X.; He, H.; Lai, Q.; Wang, C.; Yang, J.; Zhang, Y.; Fang, H.; Liao, S. Computational prediction and experimental validation of revolute joint clearance wear in the low-velocity planar mechanism. *Mech. Syst. Signal Process.* **2017**, *85*, 963–976. [CrossRef]
2. Bai, Z.F.; Zhao, J.J.; Chen, J.; Zhao, Y. Design optimization of dual-axis driving mechanism for satellite antenna with two planar revolute clearance joints. *Acta Astronaut.* **2018**, *144*, 80–89. [CrossRef]
3. Yang, L.; Zhang, X.; Huang, Y. Dynamic analysis of open-loop mechanisms with multiple spatial revolute clearance joints. *Proc. Inst. Mech. Eng. Part C-J. Mech. Eng. Sci.* **2019**, *233*, 593–610. [CrossRef]
4. Chen, X.; Jiang, S.; Wang, S.; Deng, Y. Dynamics analysis of planar multi-DOF mechanism with multiple revolute clearances and chaos identification of revolute clearance joints. *Multibody Syst. Dyn.* **2017**, *90*, 147–163. [CrossRef]
5. Carpick, R.W. The contact sport of rough surfaces. *Science* **2018**, *359*, 38. [CrossRef] [PubMed]
6. Chen, Z.; Liu, Y.; Zhou, P. A novel method to identify the scalingregion of rough surface profile. *Fractals* **2019**, *27*, 1950011. [CrossRef]
7. Lankarani, H.M.; Nikravesh, P.E. A contact force model with hysteresis damping for impact analysis of multibody systems. *J. Mech. Des.* **1990**, *112*, 369–376. [CrossRef]
8. Johnson, K.L. *Contact Mechanics*; Cambridge University Press: Cambridge, UK, 1987.
9. Li, Y.; Wang, C.; Huang, W.H. Dynamics analysis of planar rigid-flexible coupling deployable solar array system with multiple revolute clearance joints. *Mech. Syst. Signal Process.* **2019**, *117*, 188–209. [CrossRef]
10. Liu, C.S.; Zhang, K.; Yang, R. The FEM analysis and approximate model for cylindrical joints with clearances. *Mech. Mach. Theory* **2007**, *42*, 183–197. [CrossRef]
11. Wang, G.X.; Liu, C.S. Further investigation on improved viscoelastic contact force model extended based on hertz's law in multibody system. *Mech. Mach. Theory* **2020**, *153*, 103986. [CrossRef]
12. Müser, M.H.; Dapp, W.B.; Bugnicourt, R.; Sainsot, P.; Lesaffre, N.; Lubrecht, T.A.; Persson, B.N.; Harris, K.; Bennett, A.; Schulze, K.; Rohde, S. Meeting the contact mechanics challenge. *Tribol. Lett.* **2017**, *65*, 118. [CrossRef]
13. Tomota, T.; Kondoh, Y.; Ohmori, T. Modeling solid contact betweensmooth and rough surfaces with non-gaussian distributions. *Tribol. Trans.* **2019**, *62*, 580–591. [CrossRef]
14. Jackson, R.L.; Green, I. A finite element study of elastoplastic hemispherical contact against a rigid flat. *J. Tribol.* **2005**, *127*, 343–354. [CrossRef]
15. Wang, Z.; Liu, X. Model for elastic—Plastic contact between rough surfaces. *J. Tribol.* **2018**, *140*, 051402. [CrossRef]
16. Ciavarella, M.; Decuzzi, P. The state of stress induced by the plane frictionless cylindrical contact. II. The general case (elastic dissimilarity). *Int. J. Solids Struct.* **2001**, *38*, 4525–4533. [CrossRef]
17. Wang, X.; Liu, G.; Ma, S.; Tong, R. Study on dynamic responses of planar multibody systems with dry revolute clearance joint Numerical and experimental approaches. *J. Sound Vib.* **2019**, *438*, 116–138. [CrossRef]
18. Li, J.; Yan, S.; Guo, F.; Guo, P. Effects of damping, friction, gravity, and flexibility on the dynamic performance of a deployable mechanism with clearance. *Proc. Inst. Mech. Eng. Part C J. Mech. Eng. Sci.* **2013**, *227*, 1791–1803. [CrossRef]
19. Li, H.Q.; Liu, X.F.; Duan, L.C.; Cai, G.P. Deployment and control of spacecraft solar array considering joint stick-slip friction. *Aerosp. Sci. Technol.* **2015**, *42*, 342–352. [CrossRef]
20. Zheng, E.; Wang, T.; Guo, J.; Zhu, Y.; Lin, X.; Wang, Y.; Kang, M. Dynamic modeling and error analysis of planar flexible multilink mechanism with clearance and spindle-bearing structure. *Mech. Mach. Theory* **2019**, *131*, 234–260. [CrossRef]
21. Haddouni, M.; Acary, V.; Garreau, S.; Beley, J.D.; Brogliato, B. Comparison of several formulations and integration methods for the resolution of DAEs formulations in event-driven simulation of nonsmooth frictionless multibody dynamics. *Multibody Syst. Dyn.* **2017**, *41*, 201–231. [CrossRef]
22. Tan, X.; Chen, G.; Sun, D.; Chen, Y. Dynamic Analysis of Planar Mechanical Systems with Clearance Joint Based on LuGre Friction Model. *J. Comput. Nonlinear Dyn.* **2018**, *13*, 061003. [CrossRef]
23. Hou, J.; Yao, G.; Huang, H. Dynamic analysis of a spatial mechanism including frictionless spherical clearance joint with flexible socket. *J. Comput. Nonlinear Dyn.* **2018**, *13*, 031002. [CrossRef]
24. Chen, X.; Jiang, S.; Deng, Y.; Wang, Q. Dynamics analysis of 2-DOF complex planar mechanical system with joint clearance and flexible links. *Nonlinear Dyn.* **2018**, *93*, 1009–1034. [CrossRef]
25. Zheng, X.; Zhang, F.; Wang, Q. Modeling and simulation of planar multibody systems with revolute clearance joints considering stiction based on an LCP method. *Mech. Mach. Theory* **2018**, *130*, 184–202. [CrossRef]
26. Sun, D.; Shi, Y.; Zhang, B. Robust optimization of constrained mechanical system with joint clearance and random parameters using multi-objective particle swarm optimization. *Struct. Multidiscip. Optim.* **2018**, *58*, 2073–2084. [CrossRef]
27. Qu, S.; Li, R.; Bai, S.; Liang, S. Unified model for the output accuracy of open-chain manipulators that considers joint clearance and structural parameters. *J. Mech. Sci. Technol.* **2018**, *32*, 4925–4931. [CrossRef]
28. Lu, J.; Jiang, J.; Li, J.; Wen, M. Analysis of dynamic mechanism and global response of vehicle shimmy system with multi-clearance joints. *J. Vib. Control.* **2018**, *24*, 2312–2326. [CrossRef]
29. Yu, H.; Zhang, J.; Wang, H. Dynamic performance of over-constrained planar mechanisms with multiple revolute clearance joints. *Proc. Inst. Mech. Eng. Part C J. Mech. Eng. Sci.* **2018**, *232*, 3524–3537. [CrossRef]

30. Greenwood, J.A.; Williamson, J.B.P. Contact of nominally flat surfaces. *Proc. R. Soc. Lond.* **1966**, *295*, 300–319.
31. Wang, S.; Komvopoulos, K. A fractal theory of the interfacial temperature distribution in the slow sliding reime. *J. Tribol. (ASME)* **1994**, *116*, 812–823. [CrossRef]
32. Guo, J.; He, P.; Liu, Z.; Huang, H. Investigation of an improved planar revolute clearance joint contact model with rough surface. *Tribol. Int.* **2019**, *134*, 385–393. [CrossRef]
33. Bai, Z.; Liu, T.; Li, J.; Zhao, J. Numerical and experimental study on dynamic characteristics of planar mechanism with mixed clearances. *Mech. Based Des. Struct. Mach.* **2023**, *51*, 6142–6165. [CrossRef]
34. Chen, X.; Yang, W. Dynamic modeling and analysis of spatial parallel mechanism with revolute joints considering radial and axial clearances. *Nonlinear Dyn.* **2021**, *106*, 1929–1953. [CrossRef]
35. Subbaraj, K.; Dokainish, M.A. A survey of direct time-integration methods in computational structural dynamics—II. Implicit methods. *Comput. Struct.* **1989**, *32*, 1387–1401. [CrossRef]

Disclaimer/Publisher's Note: The statements, opinions and data contained in all publications are solely those of the individual author(s) and contributor(s) and not of MDPI and/or the editor(s). MDPI and/or the editor(s) disclaim responsibility for any injury to people or property resulting from any ideas, methods, instructions or products referred to in the content.